Supplementary Information for
A hybrid-frequency on-chip programmable synthetic-dimension simulator with arbitrary couplings

Xiao-Dong Zeng,[1,2,3,*] Zhao-An Wang,[1,2,3,5,*] Jia-Ming Ren,[1,2,3,*] Yi-Tao Wang,[1,2,3,†] Chun Ao,[1,2,3] Wei Liu,[1,2,3] Nai-Jie Guo,[1,2,3,4] Lin-Ke Xie,[1,2,3] Jun-You Liu,[1,2,3,4] Yu-Hang Ma,[1,2,3] Ya-Qi Wu,[1,2,3] Shuang Wang,[1,2,3,4] Pei-Yun Li,[1,2,3] Mu Yang,[1,2,3] Jin-Shi Xu,[1,2,3,4] Xi-Wang Luo,[1,2,3,4] Jian-Shun Tang,[1,2,3,4,‡] Chuan-Feng Li,[1,2,3,4,§] and Guang-Can Guo[1,2,3,4]

[1] *Laboratory of Quantum Information, University of Science and Technology of China, Hefei 230026, China*

[2] *Anhui Province Key Laboratory of Quantum Network, University of Science and Technology of China, Hefei 230026, China*

[3] *CAS Center For Excellence in Quantum Information and Quantum Physics, University of Science and Technology of China, Hefei 230026, China*

[4] *Hefei National Laboratory, University of Science and Technology of China, Hefei 230088, China*

[5] *Quantum Science Center of Guangdong-Hong Kong-Macao Greater Bay Area, Shenzhen 518045, China*

(Dated: October 15, 2025)

CONTENTS

* These authors contributed equally to this work.
† yitao@ustc.edu.cn
‡ tjs@ustc.edu.cn
§ cfli@ustc.edu.cn

I. THEORETICAL DETAILS

A. Deriving band structures from MZI-assisted two-resonator dynamics

In this subsection, we present the theoretical details of constructing the frequency lattice using a single resonant peak, under the condition of spatially tunable coupling between two-ring resonator. Based on our previous work [1], we have provided a theoretical analysis of the method for constructing a frequency lattice using intra-resonant modes in a single resonator, and a similar approach is employed here. We let a be the annihilation operator of the ring-A resonant peak with central frequency ω_0 and a_n be the annihilation operator the n-th mode with frequency $n\Omega$. Similarly, for ring-B resonator, we define the corresponding annihilation b and b_n [2, 3]. For a and b, they satisfy $a = \frac{1}{\sqrt{N_t}} \sum_{n=-N}^{N} a_n(t)e^{-in\Omega t}$, $b = \frac{1}{\sqrt{N_t}} \sum_{n=-N}^{N} b_n(t)e^{-in\Omega t}$. We let the light be injected from Resonator A and the input-output relation can be written as:

$$
\begin{aligned}
\partial_t \sum_{n=-N}^{N} \frac{1}{\sqrt{N_t}} a_n e^{-in\Omega t} &= \sum_{n=-N}^{N} (-i\omega_0 - \gamma/2) \frac{1}{\sqrt{N_t}} a_n e^{-in\Omega t} + iJ_B^H \sum_{n=-N}^{N} \frac{1}{\sqrt{N_t}} a_n e^{-in\Omega t} + iJ^V \sum_{n=-N}^{N} \frac{1}{\sqrt{N_t}} b_n e^{-in\Omega t} \\
&\quad + iJ^C \sum_{n=-N}^{N} \frac{1}{\sqrt{N_t}} b_{n+1} e^{-i(n+1)\Omega t} + i\sqrt{\gamma_c}\, s_p e^{-i\omega_p t}, \\
\partial_t \sum_{n=-N}^{N} \frac{1}{\sqrt{N_t}} b_n e^{-in\Omega t} &= \sum_{n=-N}^{N} (-i\omega_0 - \gamma/2) \frac{1}{\sqrt{N_t}} b_n e^{-in\Omega t} + iJ_A^H \sum_{n=-N}^{N} \frac{1}{\sqrt{N_t}} b_n e^{-in\Omega t} + iJ^V \sum_{n=-N}^{N} \frac{1}{\sqrt{N_t}} a_n e^{-in\Omega t} \\
&\quad + iJ^C \sum_{n=-N}^{N} \frac{1}{\sqrt{N_t}} a_{n+1} e^{-i(n+1)\Omega t}, \\
\sum_{n=-N}^{N} \frac{1}{\sqrt{N_t}} \dot{a}_n e^{-in\Omega t} &= \sum_{n=-N}^{N} (-i\omega_0 + in\Omega - \gamma/2) \frac{1}{\sqrt{N_t}} a_n e^{-in\Omega t} + iJ_A^H \sum_{n=-N}^{N} \frac{1}{\sqrt{N_t}} a_n e^{-in\Omega t} + iJ^V \sum_{n=-N}^{N} \frac{1}{\sqrt{N_t}} b_n e^{-in\Omega t} \\
&\quad + iJ^C \sum_{n=-N}^{N} \frac{1}{\sqrt{N_t}} b_{n+1} e^{-i(n+1)\Omega t} + i\sqrt{\gamma_c} s_p e^{-i\omega_p t}, \\
\sum_{n=-N}^{N} \frac{1}{\sqrt{N_t}} \dot{b}_n e^{-in\Omega t} &= \sum_{n=-N}^{N} (-i\omega_0 + in\Omega - \gamma/2) \frac{1}{\sqrt{N_t}} b_n e^{-in\Omega t} + iJ_B^H \sum_{n=-N}^{N} \frac{1}{\sqrt{N_t}} b_n e^{-in\Omega t} + iJ^V \sum_{n=-N}^{N} \frac{1}{\sqrt{N_t}} a_n e^{-in\Omega t} \\
&\quad + iJ^C \sum_{n=-N}^{N} \frac{1}{\sqrt{N_t}} a_{n+1} e^{-i(n+1)\Omega t}.
\end{aligned}
\tag{S1}
$$

where $\gamma = \gamma_c + \gamma_{in}$ is the total decay rate which is the sum of the resonator-waveguide coupling rate and the intrinsic loss rate of the rensonator. $J_A^H (J_B^H)$, J^V and J^C represent the horizontal, vertical, and cross-coupling strengths in the model, respectively. Ω is the modulation frequency, and s_p and ω_p are the amplitude and frequency of the probing laser. For the case that $\Omega \ll \gamma$ and J, the term $in\Omega$ in Eq. (S1) can be neglected. We consider the nearest-neighbor coupling in our demonstration ($J_A^H(t) = 2J^H \cos(\Omega t + \phi_A^H)$, $J_B^H(t) = 2J^H \cos(\Omega t + \phi_B^H)$, $J^C(t) = 2J^C \cos(\Omega t + \phi_C)$, J^V =constant), and the analytical treatment of long-range coupling scenarios proceeds similarly. The large number $N_t = 2N + 1$ is the total number of lattice points. By transforming $a_n e^{i\omega_p t} \to a_n$ and denoting the detuning of the

probing laser as $\Delta\omega = -\omega_0 - \omega_p$, we have:

$$\begin{aligned}
\sum_n \dot{a}_n e^{-in\Omega t} &= (i\Delta\omega - \gamma/2)\sum_n a_n e^{-in\Omega t} + iJ^H(\sum_n a_n e^{-i(n+1)\Omega t - i\phi_A^H} + \sum_n a_n e^{-i(n-1)\Omega t + i\phi_A^H}) + iJ^V \sum_n b_n e^{-in\Omega t} \\
&\quad + iJ^C(\sum_n b_n e^{-i(n+1)\Omega t - i\phi_C} + \sum_n b_n e^{-i(n-1)\Omega t} + \phi_C) + i\sqrt{N_t}\sqrt{\gamma_c}s_p, \\
\sum_n \dot{b}_n e^{-in\Omega t} &= (i\Delta\omega - \gamma/2)\sum_n b_n e^{-in\Omega t} + iJ^H(\sum_n b_n e^{-i(n+1)\Omega t - i\phi_B^H} + \sum_n b_n e^{-i(n-1)\Omega t + i\phi_B^H}) + iJ^V \sum_n a_n e^{-in\Omega t} \\
&\quad + iJ^C(\sum_n a_n e^{-i(n+1)\Omega t - i\phi_C} + \sum_n a_n e^{-i(n-1)\Omega t + i\phi_C}).
\end{aligned} \tag{S2}$$

The equation can be solved by extracting the coefficients of the $e^{-in\Omega t}$ terms with respect to n.

$$\begin{aligned}
\dot{a}_n &= (i\Delta\omega - \gamma/2)a_n + iJ^H(a_{n-1}e^{-i\phi_A^H} + a_{n+1}e^{i\phi_A^H}) + iJ^V b_n + iJ^C(b_{n-1}e^{-i\phi_C} + b_{n+1}e^{i\phi_C}) + i\sqrt{N_t}\sqrt{\gamma_c}s_p e^{in\Omega t}\delta_{n,0}, \\
\dot{b}_n &= (i\Delta\omega - \gamma/2)b_n + iJ^H(b_{n-1}e^{-i\phi_B^H} + b_{n+1}e^{i\phi_B^H}) + iJ^V a_n + iJ^C(a_{n-1}e^{-i\phi_C} + a_{n+1}e^{i\phi_C}).
\end{aligned} \tag{S3}$$

Eq. (S3) can be rewritten in the quasi-momentum space by using transformation $a_k = \frac{1}{\sqrt{N_t}}\sum_n a_n e^{-in\Omega k}$, $b_k = \frac{1}{\sqrt{N_t}}\sum_n b_n e^{-in\Omega k}$, we have

$$\begin{aligned}
i\dot{a}_k &= (-\Delta\omega - i\gamma/2 - 2J^H\cos(k\Omega + \phi_A^H))a_k - J^V b_k - 2J^C\cos(k\Omega + \phi_C)b_k + i\sqrt{\gamma_c}s_p, \\
i\dot{b}_k &= (-\Delta\omega - i\gamma/2 - 2J^H\cos(k\Omega + \phi_B^H))b_k - J^V a_k - 2J^C\cos(k\Omega + \phi_C)a_k.
\end{aligned} \tag{S4}$$

Here we define $|\varphi_k\rangle = (a_k, b_k)^{\mathrm{T}}$, $|0\rangle = (1,0)^{\mathrm{T}}$ and $|1\rangle = (0,1)^{\mathrm{T}}$. The above equation can be written as:

$$-\left[\Delta\omega + i\gamma/2 - H_k(t) + i\partial_t\right]|\varphi_k\rangle = \sqrt{\gamma_c}T\delta(t-k)s_p\,|0\rangle\,. \tag{S5}$$

The Hamiltonian in the k-space is:

$$H_k = -2\begin{bmatrix} J^H\cos(k\Omega + \phi_A^H) & J^V/2 + J^C\cos(k\Omega + \phi_C) \\ J^V/2 + J^C\cos(k\Omega + \phi_C) & J^H\cos(k\Omega + \phi_B^H) \end{bmatrix}. \tag{S6}$$

This exactly corresponds to the k-space Hamiltonian of the Creutz ladder. When $t = k$ is sufficiently larger than $1/\gamma$, the system evolves to a steady state, and the steady-state solution of Eq. (S4) can be obtained. Let ψ_i be the eigenstate of H_k, then:

$$\langle\psi_i\,|\Delta\omega + i\gamma/2 - H_k|\,\varphi_k\rangle = -\sqrt{\gamma_c}s_p\langle\psi_i|0\rangle. \tag{S7}$$

Let E_i be the eigenvalue of H_k, then:

$$(\Delta\omega + i\gamma/2 - E_i)\,\langle\psi_i\mid\varphi_k\rangle = -\sqrt{\gamma_c}s_p\,\langle\psi_i\mid 0\rangle\,. \tag{S8}$$

So we can obtain:

$$\langle\psi_i|\varphi_k\rangle = \frac{-\sqrt{\gamma_c}s_p\,\langle\psi_i|0\rangle}{\Delta\omega + i\gamma/2 - E_i} \tag{S9}$$

Thus, we can obtain the expression of a_k:

$$a_k = \langle 0 \mid \varphi_k \rangle = \langle 0 \mid \psi_1 \rangle \langle \psi_1 \mid \varphi_k \rangle + \langle 0 \mid \psi_2 \rangle \langle \psi_2 \mid \varphi_k \rangle = -\left(\frac{\sqrt{\gamma_c} s_p \left| \langle 0 \mid \psi_1 \rangle \right|^2}{\Delta\omega + i\gamma/2 - E_1} + \frac{\sqrt{\gamma_c} s_p \left| \langle 0 \mid \psi_2 \rangle \right|^2}{\Delta\omega + i\gamma/2 - E_2} \right). \tag{S10}$$

Now we obtain the expression for transmittance as follows:

$$T_{out} = \left| \frac{1}{s_p} e^{i\omega_p t} i\sqrt{\gamma_c} \sum_n \frac{1}{\sqrt{N_t}} a_n e^{-in\Omega t} \right|^2 = \left| \frac{i\sqrt{\gamma_c} a_k|_{k=t}}{s_p} \right|^2 \tag{S11}$$

.

Eq. (S11) indicates that the probing laser excites one slice of the band structure.

B. Deriving the band structure of the Su-Schrieffer-Heeger model

In this subsection, we will explain how to construct the Su-Schrieffer-Heeger (SSH) model using our approach. In the previous subsection, we always align the mode frequencies of the two resonators. However, we can intentionally shift them by δ ($\delta < \Omega_R/2$) through a DC signal applied to the resonator. As shown in Fig. 4A in the main text, J^V is changed to a modulation applied to the MZI with frequency δ, while J^C transforms into modulations with frequencies $\Omega_R + \delta$ and $\Omega_R - \delta$ applied to the MZI. We integrate this method with the intra-resonant frequency-lattice scheme. Considering two resonators with a center-frequency difference of δ and employed with two modulation frequencies $\delta - \Omega$ and δ ($\Omega \ll \gamma$), we have

$$\begin{aligned}
\frac{1}{\sqrt{N_t}} \sum_n \dot{a}_n e^{-in\Omega t} &= (-i\omega_0 + in\Omega - \gamma/2) \frac{1}{\sqrt{N_t}} \sum_n a_n e^{-in\Omega t} + i(2J_1^C \cos(\delta t) + 2J_2^C \cos((\delta - \Omega)t)) \sum_n \frac{1}{\sqrt{N_t}} b_n e^{-in\Omega t} + i\sqrt{\gamma_c} s_p e^{-i\omega_l} \\
\frac{1}{\sqrt{N_t}} \sum_n \dot{b}_n e^{-in\Omega t} &= (-i(\omega_0 + \delta) + in\Omega - \gamma/2) \frac{1}{\sqrt{N_t}} \sum_n b_n e^{-in\Omega t} + i(2J_1^C \cos(\delta t) + 2J_2^C \cos((\delta - \Omega)t)) \sum_n \frac{1}{\sqrt{N_t}} a_n e^{-in\Omega t}.
\end{aligned} \tag{S12}$$

Here, a_n and b_n are the intra-resonant frequency modes of the two resonators, J_1^C and J_2^C represent the modulation amplitudes of the two modulations applied to the MZI, and the definitions of other parameters remain consistent with those in Subsection A. Following a similar approach, we perform the transformation $a_n e^{i\omega_p t} \to a_n$ and $b_n e^{i(\omega_p + \delta)} \to b_n$, define $\Delta\omega = -\omega_0 - \omega_p$, and neglect the $in\Omega$ term. After simplification, we obtain

$$\begin{aligned}
\sum_n \dot{a}_n e^{-in\Omega t} &= (-i\Delta\omega - \gamma/2) \sum_n a_n e^{-in\Omega t} + i(2J_1^C \cos(\delta t) + 2J_2^C \cos((\delta - \Omega)t)) \sum_n b_n e^{-i(n\Omega + \delta)t} + i\sqrt{\gamma_c N_t} s_p, \\
\sum_n \dot{b}_n e^{-in\Omega t} &= (-i\Delta\omega - \gamma/2) \sum_n b_n e^{-in\Omega t} + i(2J_1^C \cos(\delta t) + 2J_2^C \cos((\delta - \Omega)t)) \sum_n a_n e^{-i(n\Omega - \delta)t}.
\end{aligned} \tag{S13}$$

Further applying the rotating wave approximation, we retain only the terms without δ in the second summation on the right-hand side of the two equations (terms containing δ correspond to the modes jumping to the frequencies that are unsupported by the two resonators, and are effectively reflected due to mode mismatch). After simplification, we obtain

$$\begin{aligned}
\sum_n \dot{a}_n e^{-in\Omega t} &= (-i\Delta\omega - \gamma/2) \sum_n a_n e^{-in\Omega t} + i \sum_n ((J_1^C b_n + J_2^C b_{n-1}) e^{-in\Omega t} + i\sqrt{\gamma_c N_t} s_p, \\
\sum_n \dot{b}_n e^{-in\Omega t} &= (-i\Delta\omega - \gamma/2) \sum_n b_n e^{-in\Omega t} + i \sum_n (J_1^C a_n + J_2^C a_{n+1}) e^{-in\Omega t}.
\end{aligned} \tag{S14}$$

Solving the equations term by term

$$\begin{aligned}
\dot{a}_n &= (-i\Delta\omega - \gamma/2) a_n + i(J_1^C b_n + J_2^C b_{n-1}) + i\sqrt{\gamma_c N_t} s_p e^{in\Omega t}, \\
\dot{b}_n &= (-i\Delta\omega - \gamma/2) b_n + i(J_1^C a_n + J_2^C a_{n+1}),
\end{aligned} \tag{S15}$$

and rewritting them in the quasi-momentum space using transformation $a_k = \frac{1}{\sqrt{N_t}} \sum_n a_n e^{-in\Omega k}$, $b_k = \frac{1}{\sqrt{N_t}} \sum_n b_n e^{-in\Omega k}$, we have

$$\begin{aligned} \dot{a}_k &= (-i\Delta\omega - \gamma/2)a_k + iJ_1^C b_k + iJ_2^C b_k e^{i\Omega k} + \sqrt{\gamma_c} s_p, \\ \dot{b}_k &= (-i\Delta\omega - \gamma/2)b_k + iJ_1^C a_k + iJ_2^C a_k e^{-i\Omega k}. \end{aligned} \tag{S16}$$

Similarly, we define $|\varphi_k\rangle = (a_k, b_k)^{\mathrm{T}}$, $|0\rangle = (1,0)^{\mathrm{T}}$ and $|1\rangle = (0,1)^{\mathrm{T}}$. The above equations can be written as:

$$-\left[\Delta\omega + i\gamma/2 - H_k(t) + i\partial_t\right]|\varphi_k\rangle = \sqrt{\gamma_c} T\delta(t-k) s_p |0\rangle . \tag{S17}$$

The Hamiltonian in k-space is

$$H_k = \begin{bmatrix} 0 & J_1^C + J_2^C e^{i\Omega k} \\ J_1^C + J_2^C e^{-i\Omega k} & 0 \end{bmatrix}, \tag{S18}$$

Similar to the previous section, we can obtain the expressions for a_k and T_{out}.

where $G = |G| e^{i\varphi(k_f)} = J_1^C + J_2^C e^{ik_f\Omega + i\phi}$ and $\varphi(k_f) = \mathrm{Arg}(G)$ is the argument of G. Here, k_f denotes the wave vector reciprocal to the frequency dimension. The topological properties of the SSH model can be described by the Zak phase:

$$\varphi_{Zak} = \frac{1}{2}\int_{-\pi}^{\pi} \frac{\partial\varphi(k_f)}{\partial k_f}\, dk_f. \tag{S19}$$

The Zak phase takes two values, which are $\varphi_{Zak} = \pi$ for the topologically non-trivial case ($J_1^C < J_2^C$) and $\varphi_{Zak} = 0$ for the trivial case ($J_1^C > J_2^C$). The expression of the band-structure theoretical solution for the SSH model is as follows:

$$\epsilon_{k_f,m} = m\sqrt{(J_1^C)^2 + (J_2^C)^2 + 2J_1^C J_2^C \cos(k_f\Omega + \phi)}. \tag{S20}$$

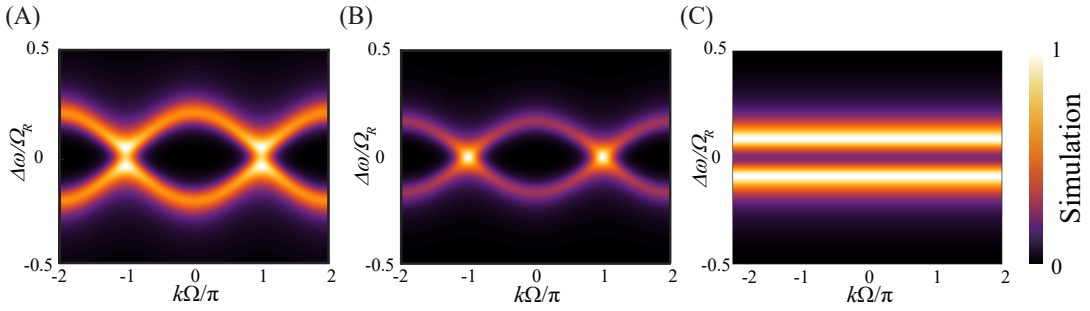

Fig. S1. **The band structure diagram is obtained from Eq. (S18) into Eq. (S11).** The band structure of the SSH model, obtained by solving the T_{out} equation derived from the coupled-mode theory, is varied via the adjustments of the parameters of J_1^C and J_2^C. Plot A-C respectively demonstrate three configurations: $J_2^C = 0.12\Omega > J_1^C = 0.08\Omega$; $J_1^C = J_2^C = 0.08\Omega$; $J_1^C = 0.08\Omega$, $J_2^C = 0$.

II. SUPPLEMENT EXPERIMENTAL DATA

A. Supplementary experimental band structure results

In this section, we present more experimental band structure data, including those from Hall ladder and Creutz ladder. In Fig. S2, we show the diverse band structures of the Hall ladder under different effective magnetic fluxes, and we also present the changes in the band structures under varying modulation strengths. In Figs. S3 and S4, we present the diverse band structures of the Creutz ladder model under different effective magnetic fluxes.

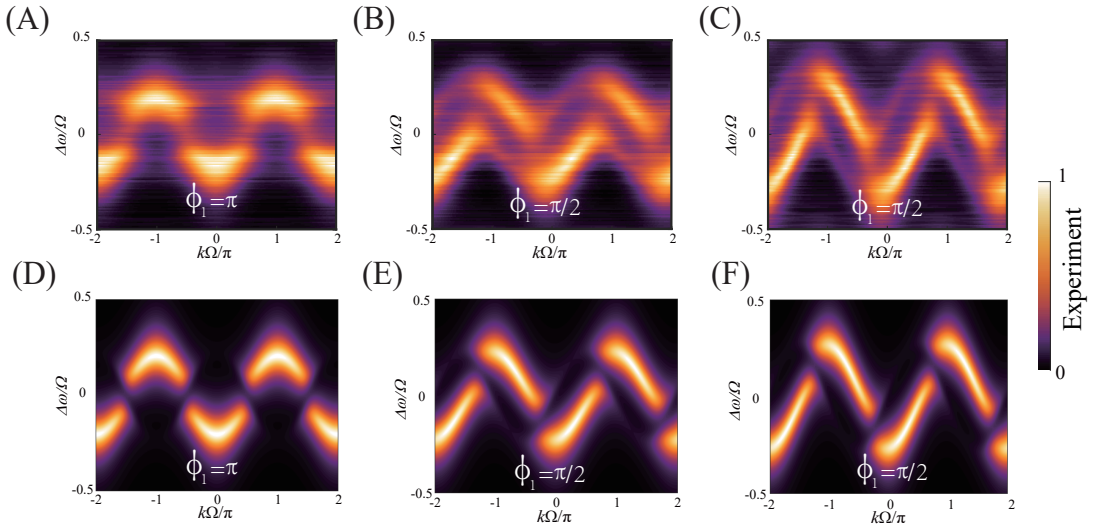

Fig. S2. **Hall ladder band structure with different effective magnetic flux (ϕ_1) and coupling strengths.** (**A**) The heat maps are the experimentally obtained band structures of Hall ladder with the coupling strength $r = J^V/2J^H = 0.8$, $J_H = 0.085\Omega_R$, $\Omega = 2\pi \times 10$ MHz, and the effective magnetic flux $\phi_1 = \pi$. (**B,C**) Band structures for effective magnetic flux $\phi_1 = \pi/2$ with couplings $r = 0.8$ and $r = 0.5$ ($J_H = 0.125\Omega_R$, $\Omega = 2\pi \times 10$ MHz). (**D-F**) Plots D-F show the numerically calculated band structure corresponding to the experimental data in the upper panels.

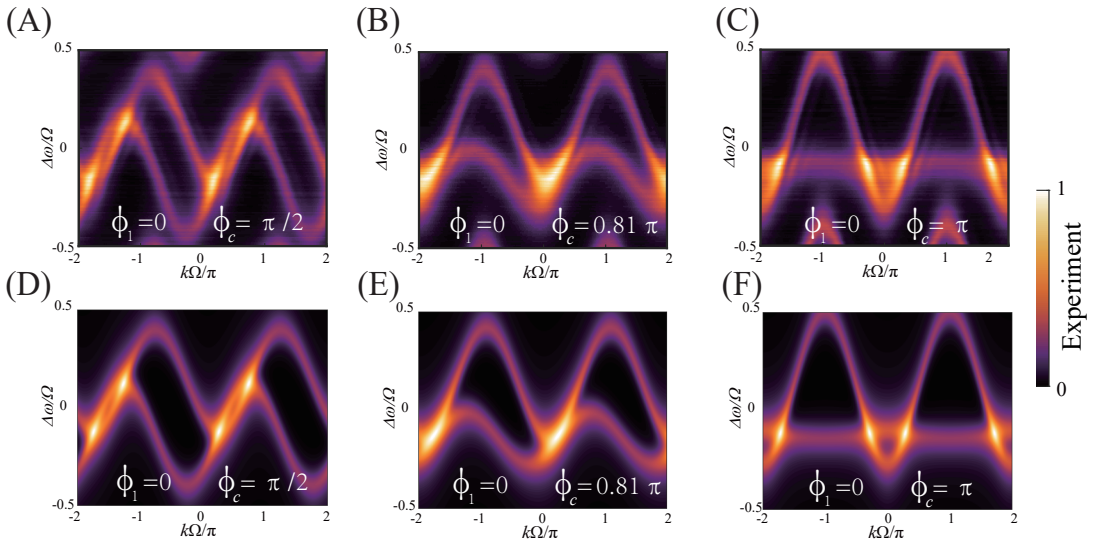

Fig. S3. **The heat maps display the band structure of the Creutz ladder with different ϕ_1 and ϕ_c.** (**A-C**) The coupling strengths are $J^V/2J^H = 0.6$, $J^C/J^H = 0.48$ and $J^H = 0.125\Omega_R$. The values of (ϕ_1, ϕ_C) corresponding to Plots A-C are $(0, \pi/2)$, $(0, 0.81\pi)$ and $(0, \pi)$, respectively. (**D-F**) Plots D-F show the numerically calculated band structure corresponding to the experimental data in the upper panels.

B. The Creutz ladder that does not form the Aharonov-Bohm cage

In order to better show the strong mode locality brought by the topological flat band, as a comparison, control experiments with zero magnetic flux ($\phi_A^H = \phi_B^H = 0$, $\phi_C = 0$, shown in the Fig. S5A) show delocalized mode distributions, confirming the absence of cage under non-topological conditions. Fig. S5B shows the band structure at this time, with obvious band crossing and no localization of photon states. Since there is no Aharonov-Bohm (AB) cage effect, namely, no constraint effect, the modes are spread out and there are higher-order frequency modes (Figs.

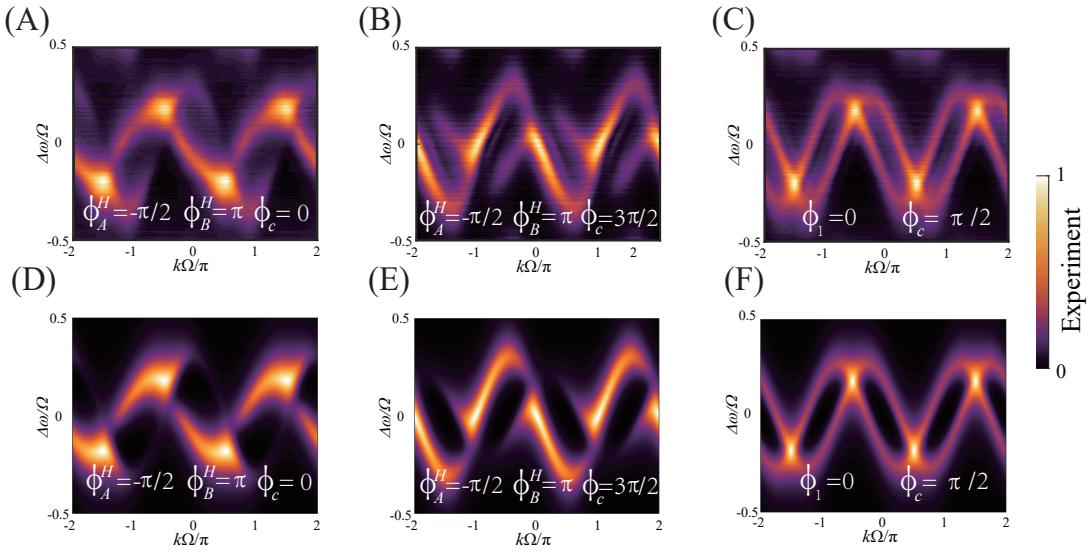

Fig. S4. **The heat maps display the band structures of the Creutz ladder with $J^V = 0$ and different ϕ_A, ϕ_B, ϕ_C (and ϕ_1).** (**A-C**) Other coupling strengths are $J^C/J^H = 1$ and $J^H = 0.11\Omega_R$. The values of (ϕ_A^H, ϕ_B^H, ϕ_C) corresponding to Plots A-C are (-π/2, π, 0), (-π/2, π, 3π/2) and (0, 0, π/2). (**D-F**) Plots D-F show the numerically calculated band structure corresponding to the experimental data in the upper panels.

S5C,D).

III. APPLICATIONS OF TOPOLOGICAL FLAT BAND IN SIDEBAND ENGINEERING

By implementing the modulated Creutz ladder lattice in the main text, the photon localization phenomenon (i.e., AB cage effect) at the topological flat band can be applied to the on-demand sideband design. Owing to the flexible construction of the intra-resonant frequency lattice, the continuous and precise sideband modulation becomes achievable, as demonstrated in Fig. S6. This rapid (depending on the electro-optic modulation rate) and deterministic optical-frequency mode conversion retains only the first-order sidebands, and the spectral structure of this localized comb is extremely simple and symmetric. In the future, this approach may have a significant impact on microwave signal generation, optical communications, precision measurements, and related fields. For example, these simple and precisely tunable frequency peaks make spectral calibration and signal processing much easier, thereby enabling high-precision measurement.

As shown in Fig. S6A, the obtained AB cage results demonstrate excellent robustness across various Ω configurations. With increasing Ω magnitude, however, the number of lattice sites in the intra-resonant lattice progressively decreases, leading to gradual degradation of the lattice system's structural integrity. Remarkably, the system maintains superior sideband tunability within the 300-MHz operational window (including a 100-MHz range with high degree of suppression of the non-demand frequencies). As shown in Fig. S6B, when the Creutz ladder model is constructed using intra-resonant frequency lattice sites and the AB cage effect is realized, the effect demonstrates notable robustness to laser detuning. This indicates that laser detuning has minimal impact on the manifestation of the AB cage effect.

IV. EFFECTIVE RANGE OF MODEL CONSTRUCTION

Attention should be paid to the fact that constructing the asymmetric coupling lattice via intra-resonant frequency lattice in our device requires control of the modulation strength. Notably, despite the initial detuning of the resonator

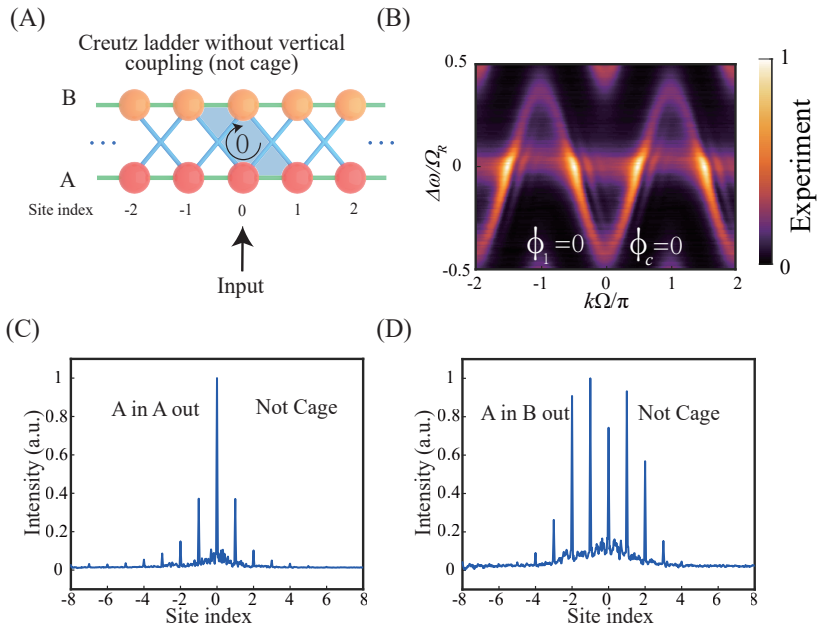

Fig. S5. **Mode distribution in the absence of AB cage effect.** (**A**) Illustration of the not-caged situation where the phase collected in the blue area is zero. The light normally spreads out along the frequency axis. (**B**) The band structure that is not the AB cage case ($\phi_A^H = \phi_B^H = 0$, $\phi_C = 0$). (**C,D**) The experimental results of the not-caged situation, where more modes survive compared to the caged situation.

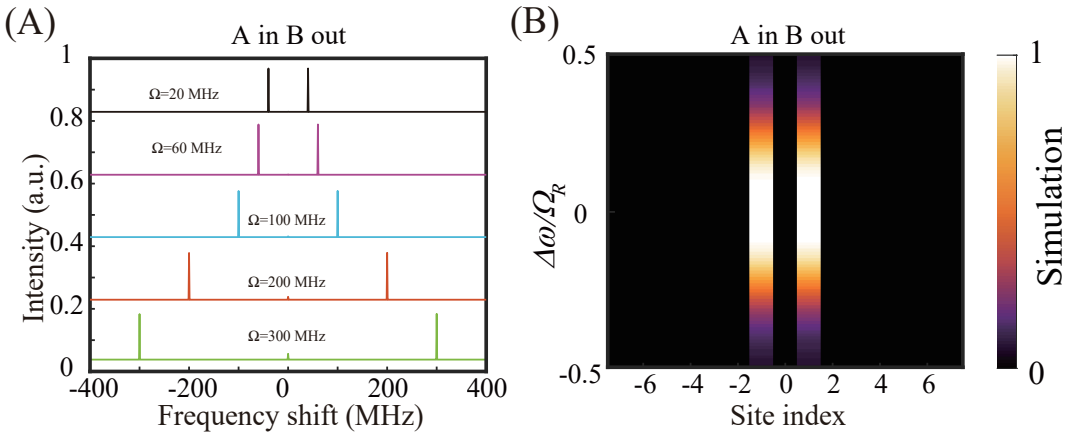

Fig. S6. **Robustness and tunability in the sideband engineering.** (A) Simulation of the mode distribution from the drop port of Resonator B when different RF signals are applied in the AB cage situation. (B) Mode distribution across the intra-resonant frequency lattice as a function of the probe-laser detuning $\Delta\omega$, measured at the drop port of Resonator B, during the emergence of the AB cage effect.

modes ($\delta > \gamma$) has suppressed the coupling between the two resonators to some extent, when excessive modulation strength is applied, the density of state (DOS) are broadened, which leads to unintended mode overlap. This phenomenon ultimately compromises the well-defined characteristics of the SSH lattice configuration. As shown in Fig. S7, the emergence of non-negligible noise within the non-band regions and the progressive degradation of the SSH-band-structure resolution are observed with increasing modulation strength. This phenomenon just originates from the mode overlap of these two resonators.

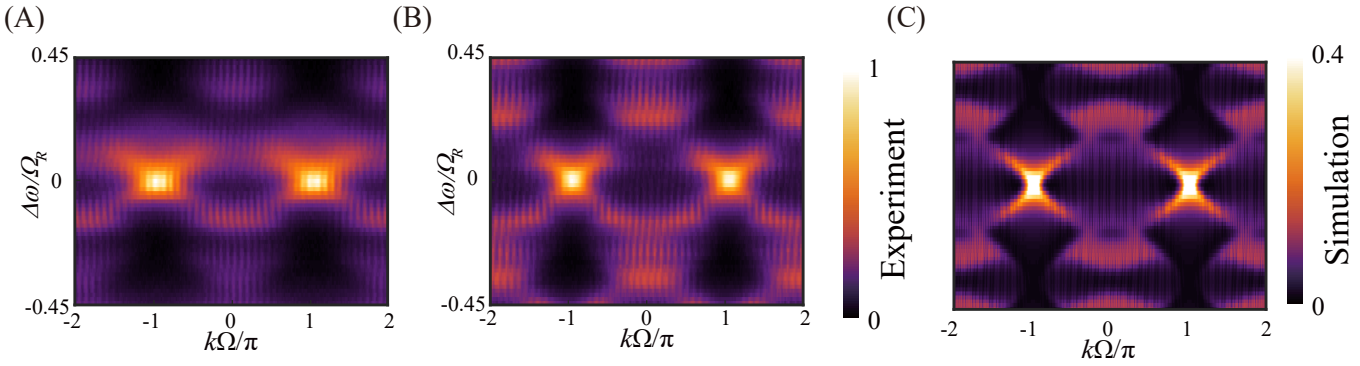

Fig. S7. **The impact of excessive modulation strength on the construction of the SSH model.** (A) Experimentally-measured stacked transmission spectra with modulation strength set at -9 dBm. (B) Experimentally-measured stacked transmission spectra with modulation strength set at -3 dBm. (C) Simulated stacked transmission spectra using photonic simulating software with modulation strength $V_{pp} = 20$ V.

V. ROBUSTNESS OF SSH LATTICE CONSTRUCTION TO FREQUENCY DETUNING

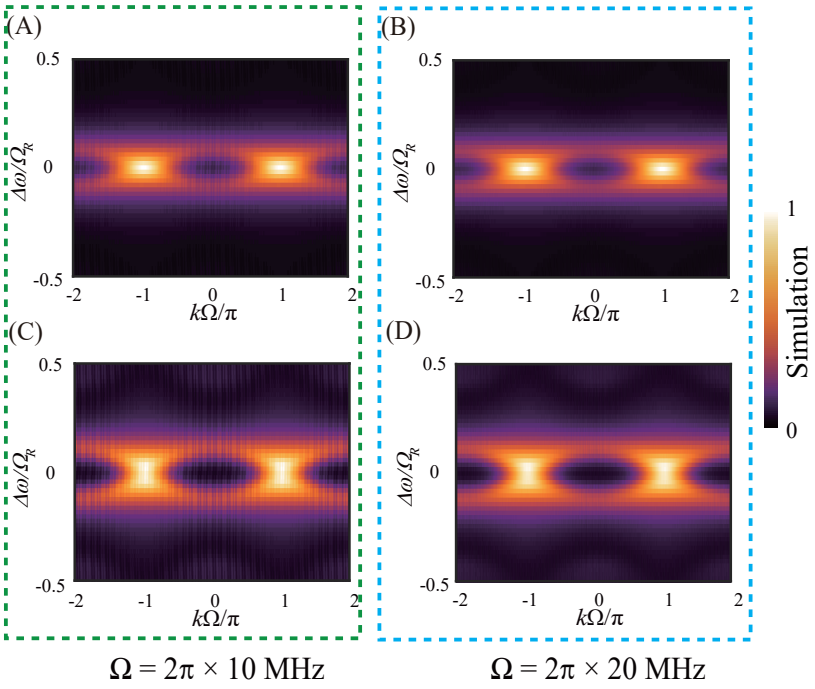

Fig. S8. **SSH band structure with different frequency separation between microwaves.** (A,C) Band structure of SSH lattice at RF modulations of $\Omega_1 = 2.5$ GHz and $\Omega_2 = 2.51$ GHz, with separation of Ω=10 MHz. (B,D) Band structure of SSH lattice at RF modulations of $\Omega_1 = 2.5$ GHz and $\Omega_2 = 2.52$ GHz, with Ω=20 MHz.

Leveraging the flexibility of construction of the intra-resonant frequency lattice, our SSH lattice implementation demonstrates robustness against the frequency detunings of the applied dual microwave signals. This robustness originates from the inherent nature of broadband and continuity of the intra-resonant frequency modes within the resonant peak, which loosens the condition of the lattice-site definition. Here, for simplicity, we consider the frequency separation between the dual microwave signals, which is related to both the detunings of these microwaves. As shown in Fig. S8, when the separation is 10 MHz, the measured band structure aligns well with the theoretical SSH model. Notably, with a 20-MHz separation, clear SSH band characteristics can still be observed. This result further highlights

the significant advantage of our approach in achieving robust on-chip asymmetric coupling lattices, particularly in demonstrating tolerance to frequency detuning of the applied microwave signals.

VI. THE CONSTRUCTION OF THE EXTEND SSH MODEL

While the SSH Hamiltonian is chirally symmetric, adding an extra coupling between neighboring sites on the same sublattice breaks the chiral symmetry, but retains inversion symmetry of the SSH lattice to give the extended SSH (xSSH) lattice. Compared to the SSH model, the xSSH model exhibits more complex and richer topological behaviors. As shown in Fig. S9A, long-range coupling can be easily implemented in our system by simply applying the RF modulation with frequency Ω to the resonators. The xSSH model Hamiltonian in the k-space is:

$$H_k = \begin{bmatrix} 2J^H \cos(\Omega k) & J_1^C + J_2^C e^{i\Omega k} \\ J_1^C + J_2^C e^{-i\Omega k} & 2J^H \cos(\Omega k) \end{bmatrix}. \tag{S21}$$

By solving the momentum-space Hamiltonian of the xSSH model, the resulting band structure is shown in Fig. S9B. Figs. S9C-F show the band structure of the xSSH model obtained with numerical simulation which correspond to the theoretical results in Fig. S9B.

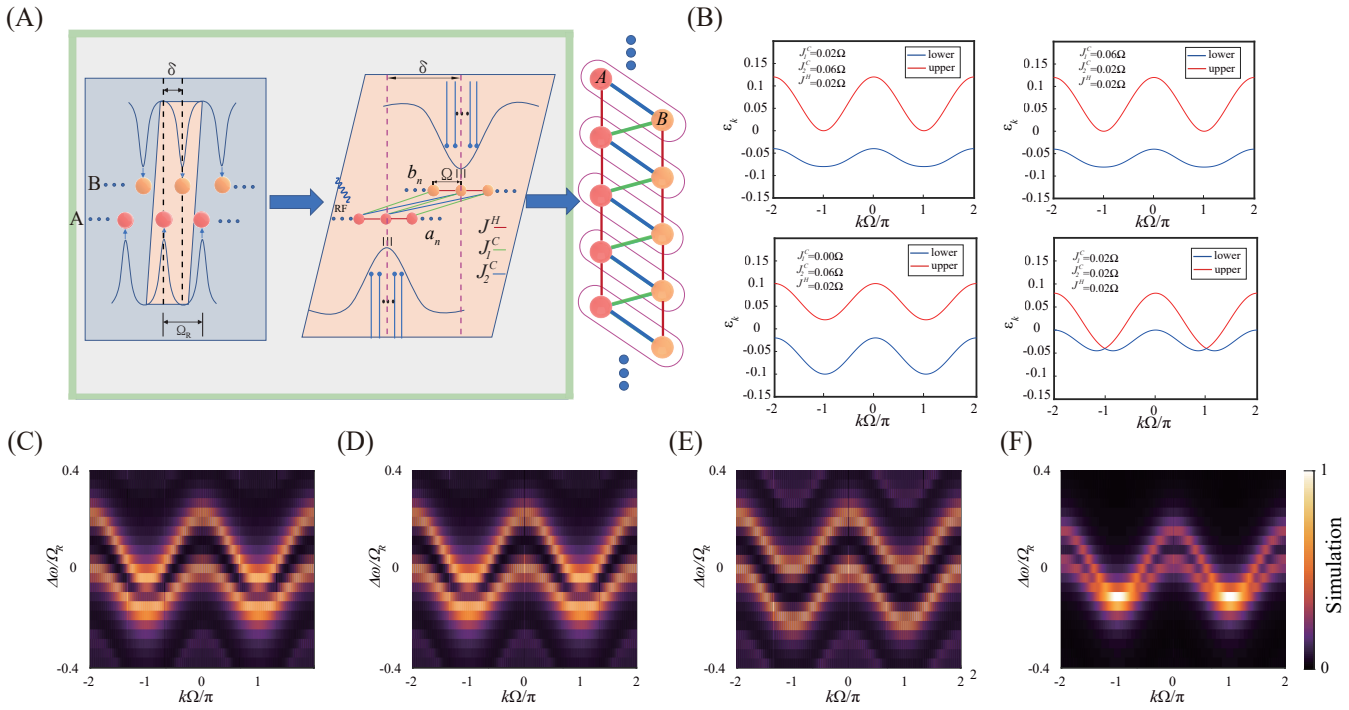

Fig. S9. **The band structure of the xSSH model.** (A) The resonant frequency peaks of Resonators A and B are detuned by δ using DC voltage. The J^H coupling is introduced by an RF modulation with frequency of Ω on the resonators. The simulation of xSSH model is realized using both the intra-resonant frequency-lattice sites and the inter-resonant sites. (B) Band structure corresponding to xSSH model, obtained by solving the k-space Hamiltonian. (C-F) Numerically-simulated solution of the xSSH model under different coupling parameters corresponding to those in Plot B.

VII. QUALITY FACTOR OF THE RESONATORS

Figs. S10 and S11 illustrate the transmission signals from the drop ports of Resonators A and B in our MZI-assisted device respectively before and after the coating of the metal. The resonators exhibit a free spectral range (FSR) of

approximately $\Omega_R = 2\pi \times 8.9$ GHz. Prior to metal deposition, the devices demonstrate a loaded quality factor of 3.7×10^5, which decreases to 1.7×10^5 after electrode fabrication due to absorption losses introduced by the metal.

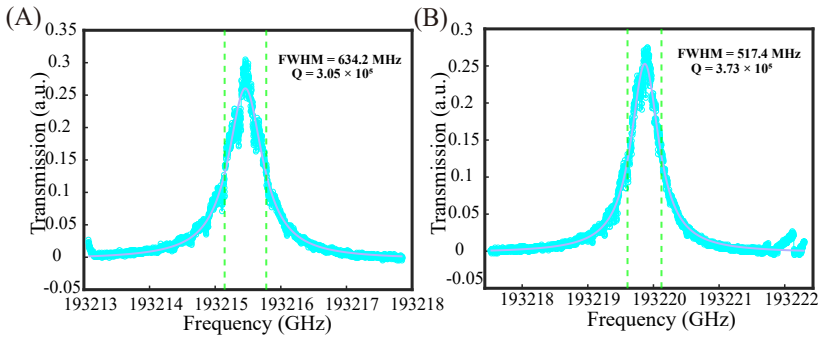

Fig. S10. **The transmission from the drop ports of Resonators A and B before the coating of the metal, respectively.**

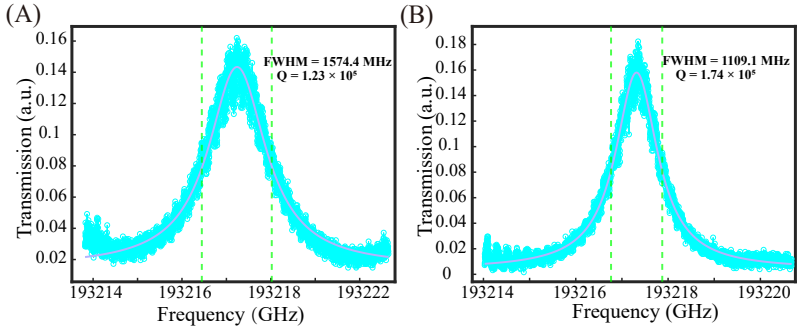

Fig. S11. **The transmission from the drop ports of Resonators A and B after the coating of the metal, respectively.**

[1] Wang, Z.-A. *et al.* On-chip photonic simulating band structures toward arbitrary-range coupled frequency lattices. *Phys. Rev. Lett.* **133**, 233805 (2024). URL https://link.aps.org/doi/10.1103/PhysRevLett.133.233805.

[2] Hu, Y., Reimer, C., Shams-Ansari, A., Zhang, M. & Loncar, M. Realization of high-dimensional frequency crystals in electro-optic microcombs. *Optica* **7**, 1189–1194 (2020). URL https://opg.optica.org/optica/abstract.cfm?URI=optica-7-9-1189.

[3] Martin, I., Refael, G. & Halperin, B. Topological frequency conversion in strongly driven quantum systems. *Phys. Rev. X* **7**, 041008 (2017). URL https://link.aps.org/doi/10.1103/PhysRevX.7.041008.